Distribution of high valence Fe sites in nickel–iron hydroxide catalysts for water oxidation

Peijia Dinga, Qi Hu, Ziwei Chaic, Hong-Bo Zhou, Guang-Hong Lu, Gilberto Teobaldi, Annabella Selloni and Li-Min Liu

Published version information

Citation: Peijia Dinga, Qi Hu, Ziwei Chaic, Hong-Bo Zhou, Guang-Hong Lu, Gilberto Teobaldi, Annabella Selloni and Li-Min Liu, Distribution of high valence Fe sites in nickel–iron hydroxide catalysts for water oxidation. ***J. Mater. Chem. A***, 2024,**12**, 2830-2838

DOI: https://doi.org/10.1039/D3TA06632K

Journal of

Materials Chemistry A

ARTICLE

Distribution of high valence Fe sites in nickel-iron hydroxide catalysts for water oxidation

Received 00th January 20xx,
Accepted 00th January 20xx

DOI: 10.1039/x0xx00000x

Peijia Ding[a], Qi Hu*[a,b], Ziwei Chai[c], Hong-Bo Zhou[a], Guang-Hong Lu[a], Gilberto Teobaldi[d], Annabella Selloni*[e] and Li-Min Liu*[a]

Nickel-iron (Ni-Fe) hydroxides have received much attention as abundant and efficient electrocatalysts for the oxygen evolution reaction (OER) under alkaline conditions. However, the behavior of Fe dopants during the reaction is still under debate. Herein, we use first-principles calculations to investigate the dehydrogenation of the basal (0001) surface of 25% Fe-doped Ni hydroxide from $Ni_{3/4}Fe_{1/4}(OH)_2$ to $Ni_{3/4}Fe_{1/4}OOH$, which is generally considered to be the active phase. Our calculations show that the high valence Fe ions tend to form domains by undergoing double-exchange processes with the neighboring Ni ions, while the oxidation states of the Ni ions do not increase steadily but fluctuate between Ni^{2+} and Ni^{3+} during the dehydrogenation. The boundaries of domains between high-valence Fe^{3+} and Fe^{4+} ions are the most reactive sites for the OER, with overpotentials as low as 0.36 V. This finding not only suggests that the abundant (0001) facet, often considered catalytically inactive in previous studies, can actually make an important contribution to the catalytic performance of nickel-iron hydroxides, but is also relevant to the design of more effective and efficient catalysts for the OER.

1. Introduction

Electrocatalytic water splitting has a central role in the conversion of renewable electricity to chemical fuels and the mitigation of current energy and environmental crises. Electrochemical water splitting involves both the reduction and oxidation of water into molecular hydrogen (H_2) and oxygen (O_2), where the kinetically slow oxygen evolution reaction (OER) – $2H_2O \rightarrow 4H^+ + O_2 + 4e^-$ (acidic conditions) or $4OH^- \rightarrow 2H_2O + O_2 + 4e^-$ (alkaline conditions) – is the bottleneck of the overall process based on the existing catalysts.[1] The development of improved low-cost and high activity OER catalysts is thus of utmost importance. Under acidic conditions, Ir-based[2,3] compounds possess excellent OER performance. However, these catalysts suffer from low abundance and high cost. Encouragingly, it has been reported that the catalytic activity of nickel hydroxide can be significantly enhanced by modifying it with other transition metals such as iron.[4–6] It has also been shown that the intrinsic catalytic activity of nickel-iron hydroxide in alkaline media is significantly higher than that of iridium-based catalysts.[7] This material can thus be an effective alternative catalyst that is both available in large quantities and relatively inexpensive.

Nickel-iron hydroxides have been investigated by various experimental techniques and computational methods.[8–14] The compositions,[4–6,9,15–17] active sites,[6,8,13,14,18–23] and mechanisms[10,24–36] have been widely examined and discussed. The most challenging and yet unsolved question remains the atomistic origin of the excellent performance reported in the experiments. For instance, Friebel *et al*. observed a 500-fold activity enhancement by replacing pure nickel hydroxide with mixed (Ni, Fe) oxyhydroxides ($Ni_{1-x}Fe_xOOH$). They further theoretically estimated overpotentials of 0.56 V for pure Ni and 0.43 V for Fe-doped γ-NiOOH $(01\bar{1}2)$ surfaces, and thus concluded that iron ions are the active sites.[19] A computational study by Li and Selloni suggested γ-NiOOH $(10\bar{1}1)$ and β-NiOOH $(01\bar{1}5)$ to be the reactive surfaces in experiments, with an overpotential of only 0.26 V for β-NiOOH $(01\bar{1}5)$.[10] Martirez *et al.* computed the overpotentials of the four-fold coordinated metal sites of β-NiOOH $(\bar{1}2\bar{1}1)$ and obtained values of 0.48 V and 0.14 V for the pure and Fe doped surfaces, respectively.[13] Goddard III *et al.* considered $\gamma\text{-}NiO_2(H_2O)_{0.66}K_{0.33}H_x$, and suggested that a synergy effect between high-valent iron and nickel ions as well as the electrolyte ions are crucial for the high OER activity.[37] Li *et al*. found that the electrodeposition of Ni^{2+} (aq) in a borate-containing electrolyte exhibits much higher OER activity than other NiO_x-based materials, and proposed that four-coordinated Ni cations are the active sites.[38] Zhang *et al.* reported a family of structurally well-defined heterobimetallic complexes, and they found that NiFe

[a]*School of Physics, Beihang University, Beijing 100191, China. E-mail: liminliu@buaa.edu.cn.*
[b]*School of Chemistry, Beihang University, Beijing 100191, China. Email: Huqi@buaa.edu.cn.*
[c]*Department of Chemistry, University of Zurich, Zurich, Switzerland*
[d]*Scientific Computing Department, STFC UKRI, Rutherford Appleton Laboratory, Harwell Campus, OX11 0QX Didcot, United Kingdom.*
[e]*Department of Chemistry, Princeton University, Princeton, NJ 08544, USA. E-mail: aselloni@princeton.edu.*
† Electronic Supplementary Information (ESI) available: See https:// DOI: 10.1039/x0xx00000x

catalyst could display significant high catalytic performance.[39] Liu *et al.* examined the incorporation of weakly bonded ligands into 3d-metal (hydro)oxides,[40] and they found that ferrum-molybdenum dual incorporated cobalt oxides could improve the performance of OER.[41]

In contrast to the high activity of nickel-iron hydroxide found in experiments, previous theoretical work reported that the overpotentials on the basal (0001) surface of Fe-doped β-NiOOH are in the range of 0.50-0.70 V and do not show any significant decrease relative to the overpotential for the undoped surface.[12,43] Previous theoretical studies of Fe doped NiOOH mostly tend to use high index surfaces rather than the basal plane to explain the experiment, such as β-NiOOH $(\bar{1}2\bar{1}1)$[13] (0.14 V), Fe-doped γ-NiOOH $(01\bar{1}2)$[19] (0.43 V), and β-NiOOH $(01\bar{1}5)$ (0.26 V)[10], respectively. However, based on the layered structure of NiOOH, the (0001) surface is the lowest energy[11,43,44] and most abundant crystallographic facet of this material[45,46] and should thus contribute significantly to the overall activity of Fe-doped NiOOH. It is therefore unclear why the calculated overpotential on this abundant facet is largely unaffected by Fe doping. A better understanding of the OER mechanism on the (0001) plane is needed in order to clarify this question and resolve the apparent discrepancy between theory and experiments.

It is widely accepted that the OER activity is closely related to the electronic structure of the active center. It was also found that the hydrogen distribution in the nickel-iron hydroxides can affect the valence state of the Ni and Fe ions. Specifically, Goldsmith *et al*. studied the electronic structure of pure Ni and mixed NiFe oxyhydroxide with different hydrogen distributions, and concluded that the Ni and Fe oxidation states are functions of the applied potential.[18] In addition, Tkalych *et al.* and Hu *et al.* considered pure β-NiOOH models with different hydrogen distributions and found that the computed OER overpotential depended strongly on such distribution.[11,35] However, most of the theoretical studies of Fe-Ni hydroxides used models constructed by simply doping Fe into nickel hydroxide without considering the hydrogen distribution.[10,13,19,47] Thus the role of the hydrogen distribution in the OER activity of these materials remains poorly understood.

In this work, we aim to obtain insights into the OER mechanism on nickel-iron hydroxide by investigating the dehydrogenation (i.e., proton-coupled oxidation) of $Ni_{3/4}Fe_{1/4}(OH)_2$ to $Ni_{3/4}Fe_{1/4}OOH$ via first-principles calculations. Our results indicate that the co-existence of neighboring Fe^{3+} and Fe^{4+} ions in partially dehydrogenated samples reduces significantly the OER overpotential to values as low as 0.36 V, which is close to the estimated theoretical limit for the OER. Our finding that the dehydrogenation has a crucial role in the high activity of nickel-iron hydroxides can be used to establish new guidelines for the development of more efficient nickel-iron hydroxide catalysts for the OER.

2. Computational methods

Density Functional Theory (DFT) calculations were performed using the projector augmented wave potentials (PAW),[48,49] as implemented in the Vienna Ab Initio Simulation Package (VASP)[50]. A plane wave kinetic energy cutoff of 500 eV was used. The generalized gradient approximation of Perdew, Burke and Ernzerhof (GGA-PBE) was chosen for the exchange-correlation (XC) functional.[51] The DFT+U method was used to correct the 3d electronic states of Ni and Fe using effective U-J terms of 5.5 and 4.3 eV obtained from linear response calculations.[52] In all calculations, van der Waals (vdW) interactions were accounted for at the D3 level.[53,54] The convergence criterion for the electronic self-consistency was 10^{-6} eV.

Because of the large number of investigated structures, a monolayer Ni-Fe hydroxide slab model was used to accelerate the analysis. This simplification (also used in previous studies, see, e.g., ref.18) has a negligible influence on the electronic structure due to the absence of covalent bonds between the hydroxide layers. The Ni:Fe ratio of 3:1 experimentally demonstrated superior catalytic performance,[4] and a 2 × 4 × 1 orthogonal supercell with 12 Ni atoms and 4 Fe atoms ($Ni_{3/4}Fe_{1/4}(OH)_2$) was employed to mimic the experimental condition. K-space was sampled using a 2 × 2 × 1 Monkhorst-Pack (MP) grid.[55] The lattice parameters of the $Ni_{3/4}Fe_{1/4}(OH)_2$ supercell were a=10.96 Å, b=12.64 Å, and c=20.35 Å; a 15 Å vacuum region was used to avoid the interaction between periodically repeated slabs. The symmetry was switched off during structural relaxation. The unit cell of the $Ni_{3/4}Fe_{1/4}(OH)_2$ during the dehydrogenation was fully optimized to release the residual stress. The structure was relaxed until the force on each atom was less than 0.01 eV/Å.

The hydrogen desorption energy, E_H, was calculated as:

$$E_H = E_{sub-deH} + \frac{1}{2}E_{H_2} - E_{sub} \quad (1)$$

where $E_{sub-deH}$ is the total energy of the structure after dehydrogenation, E_{sub} is the energy of the system before dehydrogenation, and E_{H_2} is the total energy of one H_2 molecule in vacuum. Here we simply consider energies instead of free energies because we are only interested in relative values.

As in most studies of the OER on 3d metal-based (oxy) hydroxide catalysts in alkaline media, we assumed the OER to proceed through the adsorbate evolving mechanism (AEM). This consists of the following four elementary steps:[10]

$$* + OH^- \rightarrow *OH + e^- \quad (2)$$

$$*OH + OH^- \rightarrow *O + H_2O(l) + e^- \quad (3)$$

$$*O + OH^- \rightarrow *OOH + e^- \quad (4)$$

$$*OOH + OH^- \rightarrow * + O_2(g) + H_2O(l) + e^- \quad (5)$$

where * represents an active site on the catalyst surface, $H_2O(l)$ and $O_2(g)$ denote a liquid water molecule and a gas-phase oxygen molecule, and *OH, *O, and *OOH are the adsorbed intermediates. The Gibbs free energy changes for the four steps were calculated as:[58]

$$\Delta G_1 = \Delta G_{*OH} \quad (6)$$

$$\Delta G_2 = \Delta G_{*O} - \Delta G_{*OH} \quad (7)$$

$$\Delta G_3 = \Delta G_{*OOH} - \Delta G_{*O} \quad (8)$$

$$\Delta G_4 = 4.92\ eV - \Delta G_{*OOH} \quad (9)$$

where 4.92 eV is the energy cost of splitting two water molecules into one O_2 and two H_2 molecules. The free energy differences ΔG_i and the theoretical OER overpotential (η) were determined using the computational standard hydrogen electrode scheme[56], with

$$\Delta G_i = \Delta E_i + \Delta ZPE_i - T\Delta S_i \quad (10)$$

$$\eta = \frac{1}{e}\max(\Delta G_1, \Delta G_2, \Delta G_3, \Delta G_4) - 1.23\ [V] \quad (11)$$

In Eq. (10) $\triangle E_i$, $\triangle ZPE_i$ and $\triangle S_i$ are the differences in adsorption energy, zero-point vibrational energy and vibrational entropy, respectively, and the temperature T was set at 298.15 K. The computed Gibbs free energy differences of the intermediates are listed in **Table S3**, where the energy differences ΔE_i are calculated with respect to H_2O and H_2 at potential U=0 and pH=0. The theoretical overpotential η is defined as the lowest potential at which all reaction steps are thermodynamically downhill. Further details of the OER calculations can be found in **Table S5.**

3. Results and discussion

3.1 Desorption patterns in the dehydrogenation of $Ni_{3/4}Fe_{1/4}(OH)_2$ to $Ni_{3/4}Fe_{1/4}OOH$

To identify the energetically favored pathways for the dehydrogenation of $Ni_{3/4}Fe_{1/4}(OH)_2$ to $Ni_{3/4}Fe_{1/4}OOH$, at each hydrogenation level we calculated the H desorption energy from all the inequivalent oxygen sites. We then chose the energetically favored structure at every given dehydrogenation step as the starting structure for the next step. By repeating this process, the final configuration was found. The results show that the process of H desorption from $Ni_{3/4}Fe_{1/4}(OH)_2$ to $Ni_{3/4}Fe_{1/4}OOH$ exhibits a four-stage and two-mode pathway (**Fig. 1a-d**).

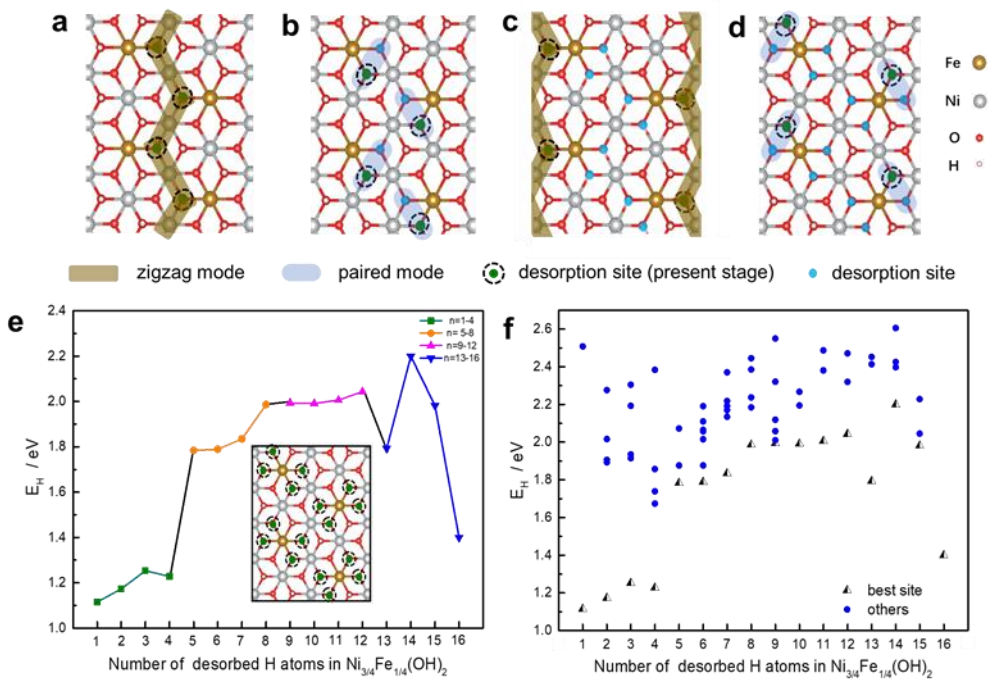

Fig. 1. Hydrogen desorption patterns in $Ni_{3/4}Fe_{1/4}(OH)_2$. (**a-d**) Atomic configurations and desorption paths in the dehydrogenation of $Ni_{3/4}Fe_{1/4}(OH)_2$ to $Ni_{3/4}Fe_{1/4}OOH$. A (2×4) supercell is considered, with the positions of the Fe dopant obtained as periodic replica of the position in the primitive cell (see **Fig. S2**). The grey, white, brown and red balls represent the Ni, H, Fe and O atoms, respectively. The brown and pale blue shaded areas highlight the zigzag and paired hydrogen desorption modes. The blue dots and green dots with dashed circles indicate the dehydrogenation sites at previous stages and present stage, respectively. (**e**) Hydrogen desorption energy (E_H) as a function of the number of desorbed H atoms in the step-by-step dehydrogenation process. (**f**) E_H as a function of the number and site of desorbed H atoms.

The first stage of dehydrogenation (n=1-4, where n indicates the number of desorbed hydrogen atoms) takes place around the four equivalent Fe positions in the supercell, resulting in a zigzag arrangement of the desorption sites (**Fig. 1a**). The first H desorption (n=1) tends to preferentially occur around the Fe rather than the Ni ions, with E_H of 1.12 eV and 2.51 eV, respectively (**Fig. 1f**). A similar pattern is observed for the second to fourth (n=2-4) H-desorption events, as depicted in **Fig. 1a** and **Fig. S3, S5**.

The second stage of dehydrogenation (n=5-8) occurs preferentially near the first-stage desorption sites (**Fig. 1b** and **Fig. S5, S6**). For example, the lowest energy desorption site for n=5 is closest to the n=1 one, with the n=1 and n=5 sites forming a pair. This pattern is replicated also for the following desorption events from n=6 to 8, with all new desorption sites paired to the previous (n=2 to 4) ones.

For the third stage of dehydrogenation (n=9-12), H exhibits a preferential desorption mode with a zigzag pattern similar to the first stage (n=1-4) (**Fig. 1c** and **Fig. S7, S8, S9**). In the final stage (n=13-16), the H desorption pattern follows the same trend as in the second stage (n=5-8), with pairing of the n=13-16 and n=9-12 desorption sites being energetically favored (**Fig. 1d** and **Fig. S10, S11**).

As shown in **Fig. 1e**, the value of the lowest E_H for each step from n=1 to 16 changes as a function of the dehydrogenation stage. For the first stage (n=1-4), E_H is in the 1.12-1.28 eV range. The hydrogen desorption takes place from the hydroxyl around the Fe ions, and the final configuration results in a zigzag pattern. For the second stage, the calculated E_H is in the 1.79-1.98 eV range, which is about 0.60-0.70 eV larger than for the first stage. The third stage also proceeds preferentially along a zigzag pattern, resulting in E_H in the range 2.00-2.05 eV for n=9-12. The final stage presents a large fluctuation in E_H for the different n's, with values varying from 1.79 eV for n=13 to 1.40 eV for n=16. After this four-stage dehydrogenation process, $Ni_{3/4}Fe_{1/4}OOH$ with an energetically favorable hydrogen distribution is eventually obtained.

3.2 Evolution of the electronic structure during the dehydrogenation of $Ni_{3/4}Fe_{1/4}(OH)_2$ to $Ni_{3/4}Fe_{1/4}OOH$

To better characterize the four-stage dehydrogenation process, we performed a detailed analysis of the electronic structure during the evolution of $Ni_{3/4}Fe_{1/4}(OH)_2$ to $Ni_{3/4}Fe_{1/4}OOH$. In the first stage, H-desorption leads to the oxidation of Fe^{2+} to Fe^{3+} (**Fig. 2b, f** and **h**). Indeed, we found that the energy-cost of the oxidation of Fe^{2+} into Fe^{3+} (1.17 eV) is significantly lower than that required for the oxidation of Ni^{2+} into Ni^{3+} (2.50 eV; see **Fig. 1f**). This may be attributed to the fact that the formation of Ni^{3+} (d^7) gives rise to a Jahn-Teller distortion whereas Fe^{3+} (d^5) does not. Thus, H desorption from the Ni site is more difficult than from the Fe site, resulting in the initial oxidation of Fe^{2+} rather than Ni^{2+}.

To determine whether the low energy cost of the oxidation of Fe^{2+} is a general characteristic of layered double hydroxides (LDH) or just a special feature of Ni-Fe hydroxides, the dehydrogenation from $X(OH)_2$ to XOOH (X=Fe, Ni, Co) was also examined. Our results show that the calculated E_H and associated transition from Fe^{2+} to Fe^{3+}, Ni^{2+} to Ni^{3+} and Co^{2+} to Co^{3+} are 1.09 eV, 1.96 eV and 1.71 eV, respectively (**Fig. S1** and **Table S1**). The 0.26 eV difference between Co^{2+} and Ni^{2+} is substantially smaller than that (0.88 eV) between Fe^{2+} and Ni^{2+}. These results suggest that the Fe doping-induced decrease of the energy cost for the first stage of the dehydrogenation is a general feature of LDHs, which is crucial for the H redistribution and appearance of Fe^{3+} in the material. It should also be noted that while the hydrogen desorption pattern and associated electronic structure may be somewhat different for different Fe doping concentrations and distributions, the general trends of the dehydrogenation process should remain largely similar.

During the second stage of the H-desorption (n=5-8), oxidation of Ni^{2+} to Ni^{3+} occurs since all the Fe^{2+} ions have previously converted into Fe^{3+}. As shown in **Fig. 2c, g** and **j**, each Ni^{3+} possesses three Ni-O bonds and three Ni-OH bonds,

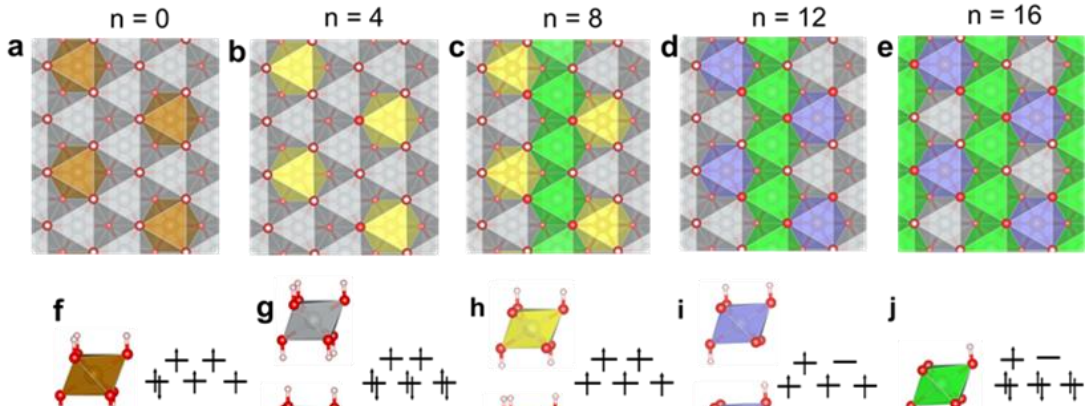

Fig. 2. Evolution of the structure and electron d orbital occupation during the dehydrogenation of $Ni_{3/4}Fe_{1/4}(OH)_2$ to $Ni_{3/4}Fe_{1/4}OOH$. At the top, n indicates the number of desorbed hydrogen atoms, where n=0 and n=16 correspond to $Ni_{3/4}Fe_{1/4}(OH)_2$ and $Ni_{3/4}Fe_{1/4}OOH$, respectively. (**a-e**) Top views for distribution of different Ni and Fe ions at each stage of the dehydrogenation process (only the upper side can be seen). (**f-j**) Octahedral crystal field and electron configuration of the inequivalent metal ions in (**a-e**).

distributed along a zigzag pattern. The electronic structure of Ni^{3+} features a singly occupied dz^2, with the long axis of the octahedra along the zigzag direction. In contrast, Fe^{3+} is coordinated with either one Fe-O and five Fe-OH bonds, or two Fe-O and four Fe-OH bonds, although the electronic configuration for the two structures is always t_{2g}^3 e_g^2.

In the third stage (n=9-12), the oxidation of Fe^{3+} is favored over that of Ni^{3+} and the residual Ni^{2+} in the systems. Thus, all the Fe^{3+} ions transform into Fe^{4+}, leaving the Ni^{3+} unchanged. The Fe^{4+} (d^4) ions exhibit high spin occupation with a shortening of Fe-O bonds in the x-y plane from 2.11 Å to 1.86 Å. Fe^{4+} is connected with three Ni-O bonds and three Ni-OH bonds (**Fig. 2i**). The energy cost of the oxidation of Fe^{3+} to Fe^{4+} is 0.44 eV lower than that of Ni^{3+} to Ni^{4+} (**Fig. S8**), indicating that Fe^{4+} is more stable than Ni^{4+}. In a previous study, Dionigi *et al*. suggested that Fe^{4+} is easier to form than Ni^{4+} (by about 0.22 eV) when considering bridging OH deprotonation in γ-NiOOH/γ-NiFe LDH.[20] Although there are no iron-oxides with Fe^{4+} ions, Fe^{4+} has been suggested by Mössbauer spectroscopy[14,57] and DFT calculations[13,37]. For instance, Mössbauer spectroscopy experiments by Chen *et al*. detected Fe^{4+} species in a 3:1 Ni:Fe layered hydroxide catalyst during steady-state water oxidation.[57] Mehmood *et al.* examined bimetallic Fe(0.38):V(0.62) nanosheets, and observed the existence of Fe^{4+} during the OER by in situ X-ray absorption spectroscopy and Fe Mössbauer spectroscopy.[14] Likewise, DFT calculations by Xiao *et al.* suggested that high-spin Fe^{4+} could lead to efficient formation of an active O radical intermediate in the active γ-phase of (Ni, Fe)OOH catalysts, with chemical formula $K_{1/3}(H_2O)_{2/3}(Ni, Fe)O_2$.[37] Using hybrid functional calculations, Martirez *et al.* found a pathway involving Fe^{4+}-oxo species (Fe^{4+}=O) in Fe-doped β-NiOOH (I2I1).[13] To match the crystal field of high spin Fe^{4+} ions ($t_{2g}^3e_g^1$) and minimize the residual stress induced by Jahn-Teller distortion, the remaining Ni^{2+} is energetically difficult to be oxidized into Ni^{3+}. (**Fig. S8** and **Table S4**). Thus, the appearance of Fe^{4+} agrees with available experimental and theoretical studies.

The evolution of the valence state for each transition metal ion during the dehydrogenation process is plotted in **Fig. 3a**. According to the trends observed for the change of valence for n=1-12, the remaining Ni^{2+} ions would be expected to become oxidized to Ni^{3+} during the final stage of the dehydrogenation (n=13-16). Instead, a complex interplay of different valence states of Fe and Ni ions is observed for n=13: three Ni^{2+} ions are oxidized to Ni^{3+}, and two Fe^{4+} ions are reduced to Fe^{3+} (**Fig. 3a**). As illustrated in **Fig. 3b,** one oxidation from Ni^{2+} to Ni^{3+} is due to the dehydrogenation from n=12 to n=13, while the other two originate from the parallel reduction of two Fe^{4+} ions to Fe^{3+} (in the areas marked by the blue dashed lines).

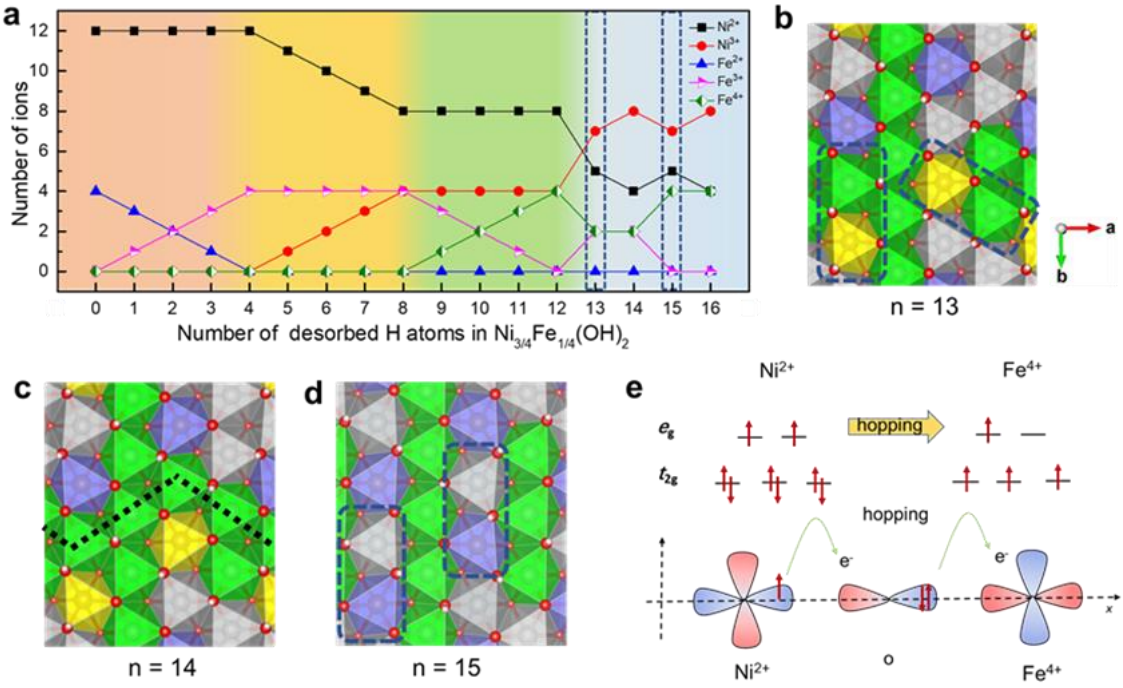

Fig. 3. Electronic structure of the transition metal ions during the dehydrogenation. (**a**) Evolution of the valence states distribution in $Ni_{3/4}Fe_{1/4}(OH)_2$ during the dehydrogenation process. The color-coded regions moving from left to right represent the different (n=1-4, n=5-8, n=9-12, and n=13-16) dehydrogenation stages; the vertical dashed blue lines highlight the special electronic structures observed for n=13 and n=15. (**b**-**d**) Evolution of the valence state distribution in $Ni_{3/4}Fe_{1/4}(OH)_2$ due to the double-exchange mechanism (n=13-15). The rectangles within the dashed blue lines in (**b**) and (**d**) are the areas where the double exchange has occurred. The black dashed line in panel **(c)** indicates the Ni^{3+} ions between Fe^{3+} and Fe^{4+}. (**e**) Schematic diagram of the double-exchange between the Fe and Ni ions. The color code for the different types of surface ions is given in **Fig. 2.**

In the step from n=13 to n=14, the usual behavior is recovered, i.e., the oxidation of Ni^{2+} to Ni^{3+} occurs with no involvement of Fe^{4+} ions. This results in a domain boundary between the Fe^{3+} and Fe^{4+} ions, with each Ni^{3+} ion being bordered by one Fe^{3+} and one Fe^{4+} (**Fig. 3c**). With further dehydrogenation to n=15, the oxidation of two Fe^{3+} to Fe^{4+} is accompanied by the reduction of two Ni^{3+} ions to Ni^{2+}, leading to the disappearance of the border between Fe^{3+} and Fe^{4+} ions. In the last step from n=15 to n=16, one Ni^{2+} is oxidized to Ni^{3+}, resulting in a final pattern with uniformly distributed Ni^{2+}, Ni^{3+} and Fe^{4+} (**Fig. 2e**). To match the crystal field of high spin Fe^{4+} ions ($t_{2g}3e_g2$) and minimize the residual stress induced by Jahn-Teller distortion, the remaining Ni^{2+} is energetically difficult to be oxidized into Ni^{3+}. The observed fluctuation in E_H at the final stage could be attributed to different electron structures. The double exchange processes occur for n=13 and 15, while an oxidation of Ni^{2+} to Ni^{3+} proceeds for n=14. As for $Ni_{3/4}Fe_{1/4}OOH$ (n=16), the distribution of H has a high symmetry, with the E_H of 1.40 eV.

Further insight into the oxidation processes occurring at n=13 and n=15 is obtained through analysis of the d orbital occupancies of Fe and Ni ions. As shown in **Fig. 3e,** the e_g orbitals of Fe and Ni are partially occupied in a high spin configuration as prescribed by Hund's rules. Direct electron hopping between the d-orbitals of adjacent Fe and Ni ions is unlikely because the distance between the two metal ions is too large. However, an indirect exchange process can occur through the 2p orbitals of the O anion in the Fe-O-Ni complex. Such a double exchange mechanism has also been found in previous studies of nickel-based oxyhydroxides.[25]

The step-by-step dehydrogenation of $Ni_{3/4}Fe_{1/4}(OH)_2$ to form $Ni_{3/4}Fe_{1/4}OOH$ results in the appearance of three oxidation states of the transition metals in the material: Fe^{4+}, Ni^{3+}, and Ni^{2+} (**Fig. 3a**), which is different from what found for pure NiOOH[11]. The coexistence of multiple valence states of Ni has been experimentally reported.[60] In order to verify the stability of the obtained $Ni_{3/4}Fe_{1/4}OOH$ structure, another $Ni_{3/4}Fe_{1/4}OOH$ model was constructed by directly doping Fe into pure β-NiOOH, so that Fe-doped β-NiOOH maintained the same H distributions of pure β-NiOOH. As reported in **Table S2**, our results show that the triple valence mixed $Ni_{3/4}Fe_{1/4}OOH$ configuration derived above by step-by-step dehydrogenation of $Ni_{3/4}Fe_{1/4}(OH)_2$ is 0.34 eV more stable than the one obtained by direct Fe doping of β-NiOOH.[11] This highlights the importance of the hydrogen distribution for Fe-doping of β-NiOOH.

3.3 The effect of the H distribution on the OER

As discussed above, the specific hydrogen distribution affects the local oxidation states of the material, which in turn results in a unique distribution of valence states at the surface of the Fe-doped

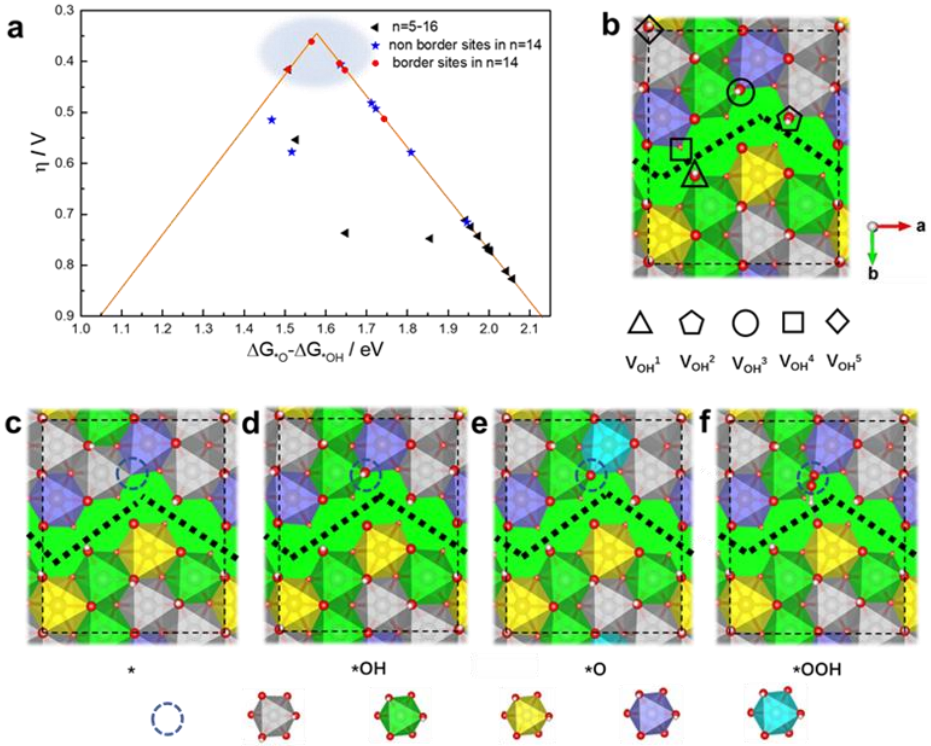

Fig. 4. OER in $Ni_{12}Fe_4O_{32}H_{32-n}$ (n=5-16). (**a**) Computed overpotential as a function of the adsorption Gibbs free energy difference $\triangle G_{*O}-\triangle G_{*OH}$ for various reactive sites during the dehydrogenation of $Ni_{3/4}Fe_{1/4}(OH)_2$; black triangles correspond to V_{OH}^4 reactive sites in $Ni_{12}Fe_4O_{32}H_{32-n}$ (n=5-16). (**b**) Locations of the five (four border and one non-border) reaction sites in $Ni_{12}Fe_4O_{32}H_{18}$ (n=14) that are at the top of the volcano plot (blue-shaded area); the corresponding free energy profiles are shown in **Fig. S12**. Locations of other investigated reaction sites in $Ni_{12}Fe_4O_{32}H_{18}$ (n=14) are shown in **Fig. S13**, and the free energies of their OER intermediates are reported in **Table S4**. (**c-f**) Oxidation-state distributions for the four intermediates of the OER at the V_{OH}^3 site with the best OER performance in $Ni_{12}Fe_4O_{32}H_{18}$ (n=14).

material. To provide a more precise characterization of how Fe doping impacts the catalytic activity, we investigated the energetics of the OER on $Ni_{12}Fe_4O_{32}H_{32-n}$ during the dehydrogenation of $Ni_{3/4}Fe_{1/4}(OH)_2$. It should be noted that lattice oxygen mechanism (LOM) and intramolecular oxygen coupling (IMOC) may also paly the vital role for the OER as suggested by the previous work.[39] To check this, the O-O coupling was also considered based on LOM and IMOC. The calculated free energies for O-O coupling are about 1.58 eV and 1.44 eV for LOM and IMOC, respectively, which prohibit the O-O coupling on the NiFe system. Thus, we considered the AEM mechanism with one hydroxyl vacancy[58] for surface configurations along the most favorable dehydrogenation pathway. Since experiments show that low valence states are unfavorable for the OER,[4] we examined the OER starting from the appearance of Ni^{3+} in n=5-16. As shown in **Fig. 4a** (black triangles, representing the $V_{OH}{}^4$ sites in n=5-16), most of the calculated overpotentials are between 0.71 V – 0.83 V and are situated on the right side of the volcano plot, with the reaction step from *OH to *O being rate-limiting. However, the calculated overpotential drops substantially to ~ 0.4 V at n=14, where the rate-limiting step becomes the O-O coupling from *O to *OOH.

To better characterize the relationship between hydrogen distribution, electronic structure and OER activity, we examined various possible reaction sites for n=14 (**Fig. 4a-b, Fig. S12**, **S13** and **Table S5**). As shown in **Fig. 4a** and **4b**, nearly all sites at the boundaries of domains between Fe^{3+} and Fe^{4+} exhibit overpotentials below 0.42 V. In particular, the site at the corner of the border region ($V_{OH}{}^3$) exhibits an overpotential of only 0.36 V, which is the smallest for all the reaction sites considered and close to the estimated theoretical limit for the AEM.[59] In contrast, the overpotentials of other regions are typically over 0.48 V (blue stars), For comparison, OER overpotentials of 0.57 V and 0.50 V on the basal plane of pure and Fe-doped NiOOH were obtained in a previous computational study that did not consider the hydrogen distribution.[43] Moreover, our calculated overpotential increased to 0.55 V and 0.74 V for n=15 and n=16, as the boundaries separating Fe^{3+} and Fe^{4+} start to disappear (at n=15) and completely disappear (at n=16). Considering the high energy cost, 0.74V, of the rate-limiting *OH → *O step for n=16, it is plausible that the border sites found at n=14 are the actual active sites for the OER in Ni-Fe hydroxides. These results clearly indicate that the special atomic and electronic structure at the border region between Fe^{3+} and Fe^{4+} is beneficial for decreasing the OER overpotential, that is, for increasing the OER activity.

The oxidation-state distributions for the four intermediates of the OER at the most favorable $V_{OH}{}^3$ site in $Ni_{12}Fe_4O_{32}H_{18}$ (n=14) are shown in **Fig. 4c-f**. First, the occurrence of an OH vacancy (V_{OH}) leads to the reduction of one Ni^{3+} to Ni^{2+}. Second, following *OH formation, one Ni^{2+} is oxidized back to Ni^{3+}. Third, upon *O formation, one Fe^{4+} is oxidized to Fe^{5+}, Here we note that while the formation of the high valence Fe^{5+} state was previously suggested by Martirez *et al*. for the OER on β-NiOOH ($\bar{1}2\bar{1}1$),[13] our results indicate that Fe^{5+} can not only form at the edge site, but also on the basal plane during the OER.

Fourth, the Fe^{5+} is reduced back to Fe^{4+} upon *OOH formation. Both iron and nickel have an effect on OER. The high-valence Fe participates in the OER reaction as the reaction center during *O and *OOH formation. Ni is mainly related with the double exchange process of Fe-O-Ni. These findings agree with in situ X-ray absorption spectroscopy and Fe Mössbauer spectroscopy results, which indicate that Fe^{4+} is the highly active species for OER.[14] Thus, the high-valent Fe in the domain, generated by dehydrogenation of the samples, is shown to play a unique role in facilitating hydroxide oxidation and boosting the OER activity. These results reduce the overpotential of basal surface and make up the shortcomings of the previous work.

4. Conclusions

We have employed first-principles calculations to investigate the OER on the basal (0001) surface of Ni-Fe hydroxides during the proton-coupled oxidation of the surface under operating conditions. Interestingly, our findings show that the catalytic activity at the often considered inert basal (0001) facet is enhanced significantly by the concerted action of high-valence Fe ions, induced by double-exchange mechanism with neighboring Ni atoms. At the same time, the valence states of the Ni ions fluctuate during the dehydrogenation process, leading to distinct boundaries between regions populated with Fe^{3+} and Fe^{4+} ions. Considering the high valence state Fe should be the active site as we discussed above, the number of active sites may be changed with the doping ratio of Fe, while the active sites should be not be affected. Our results show that OER sites located near these domain boundaries exhibit remarkably low overpotential values, with the most favorable site reaching an overpotential of only 0.36 V. These findings indicate that also the basal (0001) surface of Ni-Fe hydroxides contributes to the catalytic activity of the material, providing a new perspective of the OER mechanisms on Ni-Fe catalysts.

Author Contributions

We strongly encourage authors to include author contributions and recommend using CRediT for standardised contribution descriptions. Please refer to our general author guidelines for more information about authorship.

Conflicts of interest

There are no conflicts to declare.

Acknowledgements

The work performed at Beihang University was supported by National Natural Science Foundation of China (52225308, 11974037). L.-M.L. and G.T. acknowledge the support by the Royal Society Newton Advanced Fellowship scheme (grant No.

NAF\R1\180242). A.S. acknowledges the support of DoE-BES, Division of Chemical Sciences, Geosciences and Biosciences under award DESC0007347.

References

1 J. Suntivich, K. J. May, H. A. Gasteiger, J. B. Goodenough and Y. Shao-Horn, *Science*, 2011, **334**, 1383–1385.
2 T. Reier, M. Oezaslan and P. Strasser, *ACS Catal.*, 2012, **2**, 1765–1772.
3 L. C. Seitz, C. F. Dickens, K. Nishio, Y. Hikita, J. Montoya, A. Doyle, C. Kirk, A. Vojvodic, H. Y. Hwang, J. K. Norskov and T. F. Jaramillo, *Science*, 2016, **353**, 1011–1014.
4 L. Trotochaud, S. L. Young, J. K. Ranney and S. W. Boettcher, *J. Am. Chem. Soc.*, 2014, **136**, 6744–6753.
5 J. Zaffran, M. B. Stevens, C. D. M. Trang, M. Nagli, M. Shehadeh, S. W. Boettcher and M. Caspary Toroker, *Chem. Mater.*, 2017, **29**, 4761–4767.
6 N. Li, D. K. Bediako, R. G. Hadt, D. Hayes, T. J. Kempa, F. von Cube, D. C. Bell, L. X. Chen and D. G. Nocera, *Proc. Natl. Acad. Sci.*, 2017, **114**, 1486–1491.
7 L. Trotochaud, J. K. Ranney, K. N. Williams and S. W. Boettcher, *J. Am. Chem. Soc.*, 2012, **134**, 17253–17261.
8 M. B. Stevens, C. D. M. Trang, L. J. Enman, J. Deng and S. W. Boettcher, *J. Am. Chem. Soc.*, 2017, **139**, 11361–11364.
9 M. S. Burke, S. Zou, L. J. Enman, J. E. Kellon, C. A. Gabor, E. Pledger and S. W. Boettcher, *J. Phys. Chem. Lett.*, 2015, **6**, 3737–3742.
10 Y.-F. Li and A. Selloni, *ACS Catal.*, 2014, **4**, 1148–1153.
11 Q. Hu, Y. Xue, J. Kang, I. Scivetti, G. Teobaldi, A. Selloni, L. Guo and L.-M. Liu, *ACS Catal.*, 2022, **12**, 295–304.
12 A. Govind Rajan, J. M. P. Martirez and E. A. Carter, *J. Am. Chem. Soc.*, 2020, **142**, 3600–3612.
13 J. M. P. Martirez and E. A. Carter, *J. Am. Chem. Soc.*, 2019, **141**, 693–705.
14 R. Mehmood, W. Fan, X. Hu, J. Li, P. Liu, Y. Zhang, Z. Zhou, J. Wang, M. Liu and F. Zhang, *J. Am. Chem. Soc.*, 2023, **22**, 12206-12213.
15 M. W. Louie and A. T. Bell, *J. Am. Chem. Soc.*, 2013, **135**, 12329–12337.
16 C. Dette, M. R. Hurst, J. Deng, M. R. Nellist and S. W. Boettcher, *ACS Appl. Mater. Interfaces*, 2019, **11**, 5590–5594.
17 M. Gong, Y. Li, H. Wang, Y. Liang, J. Z. Wu, J. Zhou, J. Wang, T. Regier, F. Wei and H. Dai, *J. Am. Chem. Soc.*, 2013, **135**, 8452–8455.
18 Z. K. Goldsmith, A. K. Harshan, J. B. Gerken, M. Vörös, G. Galli, S. S. Stahl and S. Hammes-Schiffer, *Proc. Natl. Acad. Sci.*, 2017, **114**, 3050–3055.
19 D. Friebel, M. W. Louie, M. Bajdich, K. E. Sanwald, Y. Cai, A. M. Wise, M.-J. Cheng, D. Sokaras, T.-C. Weng, R. Alonso-Mori, R. C. Davis, J. R. Bargar, J. K. Nørskov, A. Nilsson and A. T. Bell, *J. Am. Chem. Soc.*, 2015, **137**, 1305–1313.
20 F. Dionigi, Z. Zeng, I. Sinev, T. Merzdorf, S. Deshpande, M. B. Lopez, S. Kunze, I. Zegkinoglou, H. Sarodnik, D. Fan, A. Bergmann, J. Drnec, J. F. de Araujo, M. Gliech, D. Teschner, J. Zhu, W.-X. Li, J. Greeley, B. R. Cuenya and P. Strasser, *Nat. Commun.*, 2020, **11**, 2522.
21 F. Bao, E. Kemppainen, I. Dorbandt, F. Xi, R. Bors, N. Maticiuc, R. Wenisch, R. Bagacki, C. Schary, U. Michalczik, P. Bogdanoff, I. Lauermann, R. van de Krol, R. Schlatmann and S. Calnan, *ACS Catal.*, 2021, **11**, 10537–10552.
22 Z. Li, M. Shao, H. An, Z. Wang, S. Xu, M. Wei, D. G. Evans and X. Duan, *Chem. Sci.*, 2015, **6**, 6624–6631.
23 C. Qiao, Z. Usman, T. Cao, S. Rafai, Z. Wang, Y. Zhu, C. Cao and J. Zhang, *Chem. Eng. J.*, 2021, **426**, 130873.
24 A. Moysiadou, S. Lee, C.-S. Hsu, H. M. Chen and X. Hu, *J. Am. Chem. Soc.*, 2020, **142**, 11901–11914.
25 B. Tian, H. Shin, S. Liu, M. Fei, Z. Mu, C. Liu, Y. Pan, Y. Sun, W. A. Goddard and M. Ding, *Angew. Chem. Int. Ed.*, 2021, **60**, 16448–16456.
26 Y. Elbaz and M. Caspary Toroker, *J. Phys. Chem. C*, 2017, **121**, 16819–16824.
27 D. Y. Chung, P. P. Lopes, P. Farinazzo Bergamo Dias Martins, H. He, T. Kawaguchi, P. Zapol, H. You, D. Tripkovic, D. Strmcnik, Y. Zhu, S. Seifert, S. Lee, V. R. Stamenkovic and N. M. Markovic, *Nat. Energy*, 2020, **5**, 222–230.
28 A. Govind Rajan and E. A. Carter, *Energy Environ. Sci.*, 2020, **13**, 4962–4976.
29 X. Wang, S. Xi, P. Huang, Y. Du, H. Zhong, Q. Wang, A. Borgna, Y.-W. Zhang, Z. Wang, H. Wang, Z. G. Yu, W. S. V. Lee and J. Xue, *Nature*, 2022, 1–7.
30 Z. He, J. Zhang, Z. Gong, H. Lei, D. Zhou, N. Zhang, W. Mai, S. Zhao and Y. Chen, *Nat. Commun.*, 2022, **13**, 2191.
31 H. Song, X. Ou, B. Han, H. Deng, W. Zhang, C. Tian, C. Cai, A. Lu, Z. Lin and L. Chai, *Angew. Chem. Int. Ed.*, 2021, **60**, 24054–24058.
32 C. Kuai, C. Xi, A. Hu, Y. Zhang, Z. Xu, D. Nordlund, C.-J. Sun, C. A. Cadigan, R. M. Richards, L. Li, C.-K. Dong, X.-W. Du and F. Lin, *J. Am. Chem. Soc.*, 2021, **44**, 18519-18526.
33 C. Kuai, Z. Xu, C. Xi, A. Hu, Z. Yang, Y. Zhang, C.-J. Sun, L. Li, D. Sokaras, C. Dong, S.-Z. Qiao, X.-W. Du and F. Lin, *Nat. Catal.*, 2020, **3**, 743–753.
34 W. Liao and G. Zhou, *Sci. China Mater.*, 2017, **60**, 664–673.
35 Y.-F. Li, J.-L. Li and Z.-P. Liu, *J. Phys. Chem. C*, 2021, **125**, 27033–27045.
36 W. Liu, X. Niu, J. Tang, Q. Liu, J. Luo, X. Liu and Y. Zhou, *Chem. Synth.*, 2023, **3**, 44.
37 H. Xiao, H. Shin and W. A. Goddard, *Proc. Natl. Acad. Sci.*, 2018, **115**, 5872–5877.
38 L.-F. Li, Y.-F. Li and Z.-P. Liu, *ACS Catal.*, 2020, **10**, 2581–2590.
39 H.-T. Zhang, Y.-H. Guo, Y. Xiao, H.-Y. Du and M.-T. Zhang, *Angew. Chem. Int. Ed.*, 2023, **62**, e202218859.
40 W. Liu, D. Zheng, T. Deng, Q. Chen, C. Zhu, C. Pei, H. Li, F. Wu, W. Shi, S.-W. Yang, Y. Zhu and X. Cao, *Angew. Chem. Int. Ed.*, 2021, **60**, 10614–10619.
41 W. Liu, W. Que, R. Yin, J. Dai, D. Zheng, J. Feng, X. Xu, F. Wu, W. Shi, X. Liu and X. Cao, *Appl. Catal. B Environ.*, 2023, **328**, 122488.
42 A. J. Tkalych, K. Yu and E. A. Carter, *J. Phys. Chem. C*, 2015, **119**, 24315–24322.
43 A. J. Tkalych, J. M. P. Martirez and E. A. Carter, *Phys. Chem. Chem. Phys.*, 2018, **20**, 19525–19531.
44 A. J. Tkalych, H. L. Zhuang and E. A. Carter, *ACS Catal.*, 2017, **7**, 5329–5339.
45 J. Kang, X. Qiu, Q. Hu, J. Zhong, X. Gao, R. Huang, C. Wan, L.-M. Liu, X. Duan and L. Guo, *Nat. Catal.*, 2021, **4**, 1050–1058.
46 J. Kang, Y. Xue, J. Yang, Q. Hu, Q. Zhang, L. Gu, A. Selloni, L.-M. Liu and L. Guo, *J. Am. Chem. Soc.*, 2022, **144**, 8969–8976.
47 J. Jiang, F. Sun, S. Zhou, W. Hu, H. Zhang, J. Dong, Z. Jiang, J. Zhao, J. Li, W. Yan and M. Wang, *Nat. Commun.*, 2018, **9**, 2885.
48 P. E. Blöchl, *Phys. Rev. B*, 1994, **50**, 17953–17979.
49 G. Kresse and D. Joubert, *Phys. Rev. B*, 1999, **59**, 1758–1775.
50 G. Kresse and J. Furthmüller, *Phys. Rev. B*, 1996, **54**, 11169–11186.
51 J. P. Perdew, J. A. Chevary, S. H. Vosko, K. A. Jackson, M. R. Pederson, D. J. Singh and C. Fiolhais, *Phys. Rev. B*, 1992, **46**, 6671–6687.
52 M. Cococcioni and S. de Gironcoli, *Phys. Rev. B*, 2005, **71**, 035105.
53 S. Grimme, J. Antony, S. Ehrlich and H. Krieg, *J. Chem. Phys.*, 2010, **132**, 154104.

54 A.-R. Allouche, *J. Comput. Chem.*, 2011, **32**, 174–182.
55 D. J. Chadi, *Phys. Rev. B*, 1977, **16**, 1746–1747.
56 E. Skúlason, V. Tripkovic, M. E. Björketun, S. Gudmundsdóttir, G. Karlberg, J. Rossmeisl, T. Bligaard, H. Jónsson and J. K. Nørskov, *J. Phys. Chem. C*, 2010, **114**, 18182–18197.
57 J. Y. C. Chen, L. Dang, H. Liang, W. Bi, J. B. Gerken, S. Jin, E. E. Alp and S. S. Stahl, *J. Am. Chem. Soc.*, 2015, **137**, 15090–15093.
58 I. C. Man, H.-Y. Su, F. Calle-Vallejo, H. A. Hansen, J. I. Martínez, N. G. Inoglu, J. Kitchin, T. F. Jaramillo, J. K. Nørskov and J. Rossmeisl, *ChemCatChem*, 2011, **3**, 1159–1165.
59 Z.-F. Huang, J. Song, S. Dou, X. Li, J. Wang and X. Wang, *Matter*, 2019, **1**, 1494–1518.
60 M. Görlin, P. Chernev, J. Ferreira de Araújo, T. Reier, S. Dresp, B. Paul, R. Krähnert, H. Dau and P. Strasser, *J. Am. Chem. Soc*., 2016, **138**, 5603–5614.